Numerical Investigation of Monodisperse Granular Flow Through an Inclined Rotating Chute

Sushil S. Shirsath, Johan T. Padding, and J. A. M. (Hans) Kuipers
Multiphase Reactors, Chemical Engineering and Chemistry, Eindhoven University of Technology, 5600 MB Eindhoven, The Netherlands

Tim W. J. Peeters
Dept. of Ironmaking R&D, Tata Steel, 1970 CA IJmuiden, The Netherlands

Herman J. H. Clercx
Dept. of Physics and J.M. Burgers Center for Fluid Dynamics, Eindhoven University of Technology, 5600 MB Eindhoven, The Netherlands

Dept. of Applied Mathematics, University of Twente, 7500 AE Enschede, The Netherlands

DOI 10.1002/aic.14535
Published online June 30, 2014 in Wiley Online Library (wileyonlinelibrary.com)

A discrete element model of spherical glass particles flowing down a rotating chute is validated against high quality experimental data. The simulations are performed in a corotating frame of reference, taking into account Coriolis and centrifugal forces. In view of future extensions aimed at segregation studies of polydisperse granular flows, several validation steps are required. In particular, the influence of the interstitial gas, a sensitivity study of the collision parameters, and the effect of system rotation on particle flow is investigated. Shirsath et al. have provided the benchmark laboratory measurements of bed height and surface velocities of monodisperse granular flow down an inclined rotating chute. With a proper choice of the friction coefficients, the simulations show very good agreement with our experimental results. The effect of interstitial gas on the flow behavior is found to be relatively small for 3-mm granular particles.
 AIChE J, 60: 3424–3441, 2014
Keywords: experimental validation, rotating chute, granular flows, Coriolis force, discrete element model

Introduction

Granular materials are among the most widely manipulated materials in the world. They play an important commercial role in many applications such as chemical engineering, civil engineering, pharmaceutical industry, agriculture, mining, metallurgical processing, and energy production. For handling such granular materials, various types of equipment are used in the industry. It has been estimated that 40% of the capacity of our industrial plants is wasted because of problems related to the transport of such materials.[1] Therefore, it is clear that a better understanding of the behavior of granular materials and their flow properties is of utmost importance, not only from an industrial point of view but also for geophysical applications and out of scientific curiosity. Comprehensive historical reviews of handling technologies and methodologies that had been designed from the engineering point of view are available in literature.[2]

Many industrial applications concern the processing of granular materials where particle properties, such as size, density, and shape change. During the processing steps (transportation, charging, discharging, etc.) in such applications segregation may occur, which is undesirable when a homogeneous mixture is required in, for example, the metallurgical and pharmaceutical industries.

In blast furnaces operated in the metallurgical industry, granular materials such as coke and pellets are charged from the top of a hopper into the blast furnace through an inclined rotating chute. Such particulate flows can segregate during the hopper discharge process and on the rotating chute as a result of differences in material density, size, and shape. Thus, a better understanding of the (fundamental) phenomena, allowing for a better control of the flow behavior of granular materials on the rotating chute, is very important for efficient operation of a blast furnace. The first step toward generating this understanding is to study monodisperse granular spherical particles on an inclined rotating chute by employing laboratory experiments and numerical studies of model systems.

Many previous studies have focused on granular flows through nonrotating chutes.[3–6] Some work on measurement of the velocity of different types of granular particles flowing slowly through an inclined open chute has been reported previously.[7] Augenstein and Hogg investigated the behavior of thin layers of granular particles on inclined surfaces and measured velocity profiles for different angles of inclination,

Correspondence concerning this article should be addressed to J. T. Padding at j.t.padding@tue.nl.

particle size, and chute surface.[8] They described the observed velocity profiles using a simple frictional force balance, that is, their model did not explicitly include bouncing and rolling of the particles. Therefore, the friction coefficient obtained in the work of Augenstein and Hogg can only be viewed as an effective one, lumping all effects of bouncing and rolling into a single number. A disadvantage of such an approach is that the effective friction must be tuned for each particle size and only applies to shallow granular flows.

To achieve a better understanding of the behavior of granular flows in rotating chutes, we have performed laboratory experiments [bed height measurements with sensors, particle velocity measurements at the surface of the granular flow with Particle Image Velocimetry (PIV)] and applied a discrete element model (DEM) for numerical studies. In such a numerical model, each individual particle and its collisions with neighboring particles is tracked deterministically in time. The experimental measurements (and applied techniques) and numerical simulations are strongly complementary as numerical studies give access to regions of the granular flow hidden from standard optical diagnostics. However, before we can exploit this complimentarity, a strong cross-validation of both methods is required, which will be the focus of this article.

Once validated, DEM models are one of the most useful and reliable simulation tools for the numerical analysis, flow visualization, and in-depth studies of closure relations for granular flow behavior during transport.[9–11] DEM can also provide useful information about the optimization of particulate processes. Several studies on the iron making process have already been published.[12–17] An in-house version of our discrete element method that is usually used for gas-solid fluidized beds,[18–21] has been modified to allow for the simulation of particle flows through a chute rotating around an axis parallel to gravity.

DEM simulations have also been extensively applied to study different granular flows in industries, for example, in drum mixers,[22,23] for fluidized beds,[24,25]for hopper charging, and discharging flows.[26–28] In the work related to flow in chutes, Mio et al. experimentally investigated size segregation of sintered ore particles flowing along an inclined chute for validation of DEM results.[29] Zhang et al. studied the size segregation of sintering material flows down a rough chute, simulating four types of representative particles of different diameters and magnetism using DEM modeling.[30] Mio et al. also studied particle behavior in an inclined rotating chute using DEM and observed enhanced effective particle velocities in the chute (while moving toward the outlet) due to the centrifugal force.[31] Sawley et al. studied how different ways of charging the granular material onto the vessel leads to different segregation flow and distribution of grain size using DEM simulations.[32] Some recent experimental studies and DEM simulations of granular flows in inclined rotating chutes and in the hopper was reported in the articles and thesis of Yu.[33–35]

As mentioned above, the motivation of the current analysis is to perform a cross-validation between laboratory measurements and DEM simulations of the granular flow patterns in an inclined rotating chute. We will perform this cross-validation for two fixed angles of inclination and different rotation rates of the chute. We study flow of 3-mm spherical glass particles down an inclined rotating chute by detailed DEM simulations with emphasis on the influence of the interstitial gas, a sensitivity study of the collision parameters such as restitution and (rolling) friction coefficients, and the effect of rotation on inlet particle flow. The results are validated by comparison with datasets from well-defined experiments for a fixed angle of inclination and different rotation rates of the chute.

This article is organized as follows: first, we give a summary of the simulation model and the parameter settings, then we give a brief explanation of the computational analog for calculation of the bed height and surface velocity, then we discuss the cross-validation with regards to particle charging and the choice of suitable restitution and (rolling) friction coefficients, and investigate the influence of interstitial gas. The main part of our work is focused on validation of the DEM simulations by comparing with high quality experimental data obtained by Shirsath et al.[36] After validating the model, we present computational measurements of quantities which are not readily accessible in optical experiments. Finally, we give our conclusions.

Simulation Model

The discrete element method (DEM) originally developed by Cundall and Strack has been used successfully to simulate the many granular flow systems.[9] Particle collisions are modeled by a soft-sphere contact model, which accounts for the energy dissipation due to inelastic particle interactions. This energy dissipation is characterized by the empirical coefficients of normal and tangential restitution and the coefficient of friction. The particle collision characteristics play an important role in the overall behavior of granular flows. For this reason, the collision properties of the particles used in our experimental study were accurately determined by detailed single-particle impact experiments for the normal and tangential restitution coefficients. We have estimated the coefficient of friction between particle-wall and particle–particle to achieve good agreement with result for granular flow in the nonrotating chute at an inclination angle of 30°. Then, we validate the model for other inclination angles and rotating chutes. We will show that with this coefficient of friction, good agreement is found with nonrotating and rotating granular flow experiments. We will also describe how we have adapted the equations of motion to take into account the pseudoforces that appear in a corotating frame of reference. For some simulations, we have included the effects of interstitial gas by coupling the particles to a continuum gas phase. We will describe the gas-phase equations. These equations have been incorporated in our in-house simulation codes. Let us now start with defining the equations of motion for the particles.

Equations of motion

In DEM, the particle phase is described by Newtonian equations of motion for each particle in the system. The translational and rotational equations of motion for a particle a are given by

$$m_a \frac{d\boldsymbol{v}_a}{dt} = m_a \boldsymbol{g} + \mathbf{F}_a^c + \mathbf{F}_a^p + \mathbf{F}_a^d \tag{1}$$

$$I_a \frac{d\boldsymbol{\omega}_a}{dt} = \mathbf{T}_a + \mathbf{T}_{r,a} \tag{2}$$

where m_a is the mass of particle a, $\boldsymbol{v}_a$ is the particle velocity, $\boldsymbol{\omega}_a$ is the rotational velocity, and I_a the moment of inertia

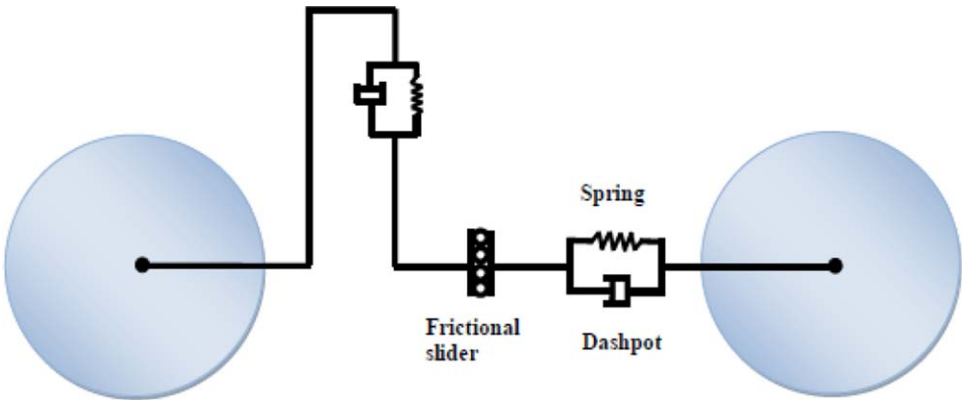

Figure 1. Schematic representation of the linear spring/dashpot soft-sphere model.

The contact force between a pair of particles is decomposed into parallel and tangential components. For each component, we define a spring and dashpot to calculate the force. The transition between a sticking and sliding collision is controlled by the coefficient of friction, which poses an upper limit to the tangential force. [Color figure can be viewed in the online issue, which is available at wileyonlinelibrary.com.]

around its center-of-mass. The first two terms on the right-hand side of Eq. 1 represent, respectively, the forces due to gravity ($\boldsymbol{g}$ is the gravitational acceleration), and forces due to direct contact with other particles and walls. The particles are coupled with the surrounding gas phase through the third and fourth term which represents, respectively, the force due to pressure gradients in the gas phase and the drag force with the gas. $\mathbf{T}_a$ is the torque on particle a, which is determined by the contact forces and $\mathbf{T}_{\mathrm{r},a}$ is the rolling torque due to rolling friction, both of which will be explained in the next section.

Soft-sphere contact model

The particle–particle and particle-wall contact force model accounts for the energy dissipated during collisions, as characterized by empirical coefficients of normal and tangential restitution, the coefficient of friction, and coefficient of rolling friction. Apart from the rolling friction, we use a standard linear spring/dashpot model, in which separate springs and dashpots are defined for both normal and tangential displacements.[9] A schematic representation of the linear spring/dashpot soft-sphere model is shown in Figure 1.

In detail, the total contact force on particle a is given as a sum of pair forces with all neighboring particles with which particle a is overlapping. The overlap (in the normal direction) between particle a and a neighbor b is defined as $\delta_{\mathrm{n}}=R_b+R_a-|\mathbf{r}_b-\mathbf{r}_a|$. The contact force on particle a in the normal direction due to this contact is given by

$$\mathbf{F}_{\mathrm{n},ab}=-k_{\mathrm{n}}\delta_{\mathrm{n}}\mathbf{n}_{ab}-\eta_{\mathrm{n}}\mathbf{v}_{\mathrm{n},ab} \tag{3}$$

where k_{n} is the normal spring stiffness, $\mathbf{n}_{ab}=(\mathbf{r}_b-\mathbf{r}_a)/|\mathbf{r}_b-\mathbf{r}_a|$ is the unit vector pointing from a to b, η_{n} is the normal damping coefficient, and $\mathbf{v}_{ab,\mathrm{n}}=(\mathbf{v}_{ab}\cdot\mathbf{n}_{ab})\mathbf{n}_{ab}$ is the normal component of the relative velocity between particles a and b at the point of contact. This relative velocity is given by

$$\mathbf{v}_{ab}=\mathbf{v}_a-\mathbf{v}_b+(R_a\boldsymbol{\omega}_a+R_b\boldsymbol{\omega}_b)\times\mathbf{n}_{ab} \tag{4}$$

For the tangential component of the contact force, a similar expression is used

$$\mathbf{F}_{\mathrm{t},ab}=-k_{\mathrm{t}}\boldsymbol{\delta}_{\mathrm{t}}-\eta_{\mathrm{t}}\mathbf{v}_{\mathrm{t},ab} \tag{5}$$

where k_{t} is the tangential spring stiffness, η_{t} is the tangential damping coefficient, and $\mathbf{v}_{ab,\mathrm{t}}=\mathbf{v}_{ab}-\mathbf{v}_{ab,\mathrm{n}}$ is the tangential component of the relative velocity. The tangential overlap $\boldsymbol{\delta}_{\mathrm{t}}$ is the time integral of this tangential velocity from the time of initial contact.[17] The above tangential force, Eq. 5, applies to the case of a sticking collision where the two surfaces in contact stick together when the tangential forces are not too large. If, however, the following relation is satisfied

$$|\mathbf{F}_{\mathrm{t},ab}|>\mu|\mathbf{F}_{\mathrm{n},ab}| \tag{6}$$

where μ is the coefficient of friction, then the two surfaces in contact start to slide relative to each other. In that case, the tangential force is limited and replaced by

$$\mathbf{F}_{\mathrm{t},ab}=-\mu|\mathbf{F}_{\mathrm{n},ab}|\mathbf{t}_{ab} \tag{7}$$

where $\mathbf{t}_{ab}=\mathbf{v}_{ab}/|\mathbf{v}_{ab}|$ is the unit vector in the tangential direction.

Although it may appear that up to this point we have to define five contact parameters ($k_{\mathrm{n}}, k_{\mathrm{t}}, \eta_{\mathrm{n}}, \eta_{\mathrm{t}}$, and μ), the number of free parameters is reduced by one by the consistency requirement that the collision time in the normal direction is the same as in the tangential direction. Using analytic solutions of the damped harmonic oscillator equations for the normal and tangential directions, it is possible to eliminate, for example, the tangential spring stiffness k_{t}. Furthermore, the analytical solutions allow us to calculate the coefficients of restitution e_{n} and e_{t} (ratio of postcollisional and precollisional velocity) for the normal and tangential directions. In practice, we, therefore, invert the equations, and use e_{n} and e_{t} as input parameters, rather than the damping coefficients because the latter are more difficult to obtain experimentally. For full details, the reader is referred to Van der Hoef et al.[19]

The resulting force and torque for particle a are obtained by adding the pairwise contributions of all the particles b that are in contact with particle a

$$\mathbf{F}_a^{\mathrm{c}}=\sum_b\left(\mathbf{F}_{\mathrm{n},ab}+\mathbf{F}_{\mathrm{t},ab}\right) \tag{8}$$

and

$$\mathbf{T}_a=\sum_b\left(R_a\mathbf{n}_{ab}\times\mathbf{F}_{\mathrm{t},ab}\right) \tag{9}$$

We note that contact forces and torques between particles and walls are treated similarly to particle–particle contacts,

but the walls are assumed to be nonmoving (in the corotating frame of reference) and of infinite mass.

Sakaguchi et al. first introduced the rolling friction concept into DEM when they performed a comparison study of experiments and modeling of plugging of granular material during silo discharge.[37] Their rolling friction model was based on a experimental and theoretical study of Beer and Johnson[38] and proposed by Zhou et al.[39] We include a rolling friction in our DEM simulation method to account for the fact that real particles are never perfectly spherical, or remain spherical upon contact. Indeed, particles in industrial processes such as in the steel industry tend to have a very irregular shape. The most accurate solution would be to model the exact particle shape. However, this is computationally very expensive because of the large increase in the number of degrees of freedom, and more expensive statistical ensemble averaging. Simulating the exact shape is, therefore, not suitable for simulating large scale granular flow in industrial processes. The particle shape mainly affects the particle rotation velocity and the particle packing fraction. As a first approximation, we will still treat the particles as spherical, but with an additional rolling friction to account for the decrease in rotation velocity.[39] To this end, we introduce an additional rolling resistance torque on a particle a due to interactions with a particle b, as follows

$$\mathbf{T}_{\mathrm{r},ab} = -\mu_{\mathrm{r}} R_{\mathrm{r}} F_{\mathrm{n},ab} \frac{\boldsymbol{\omega}_{\mathrm{rel}}}{|\boldsymbol{\omega}_{\mathrm{rel}}|} \tag{10}$$

$$\boldsymbol{\omega}_{\mathrm{rel}} = \boldsymbol{\omega}_a - \boldsymbol{\omega}_b \tag{11}$$

where $\boldsymbol{\omega}_{\mathrm{rel}}$ is the relative angular velocity between particles a and b. The rolling resistance torque is assumed to scale linearly with the magnitude of the normal force between particles a and b, and with the rolling radius R_{r} defined as

$$R_{\mathrm{r}} = \frac{R_a R_b}{(R_a + R_b)} \tag{12}$$

The dimensionless coefficient of friction μ from the soft-sphere model and the coefficient of rolling friction μ_{r} from the above model together determine the rolling behavior of a single particle falling down a plane inclined at an angle θ. For a perfectly smooth and infinitely stiff sphere, we have $\mu_{\mathrm{r}} = 0$, and the friction μ at the surface of the sphere causes a pure rolling motion without sliding for shallow inclination angles $\tan\theta < \mu$, and rolling and sliding for steeper inclination angles $\tan\theta > \mu$. For less ideal, but still nearly spherical particles, we have $0 < \mu_{\mathrm{r}} < \mu$, and the particle will repose (neither slide nor roll) for $\tan\theta < \mu_{\mathrm{r}}$, roll for $\mu_{\mathrm{r}} < \tan\theta < \mu$, and roll and slide for $\tan\theta > \mu$. Note that in our work, to ensure a continuous flow without stagnation, we will keep the inclination angle of the chute fixed at an angle for which $\tan\theta > \mu$. However, the above classification is valid only for a single particle falling down an inclined plane; the effect of rolling resistance on the flow of multiple particles is more difficult to predict and, therefore, part of this study.

Coriolis and centrifugal forces

The particles flowing through the chute are in relative motion with respect to the chute boundary, which in its turn is rotating with respect to a fixed frame. Although it is possible to simulate a moving chute boundary, for pure chute flow it is computationally more efficient to work in a frame of reference that corotates with the rotating chute. The first advantage is that contact detection between particles and the chute inner wall, as well as computation of the particle-wall contact forces, can be carried out without the need to find the location of the chute moving boundary during each computational step. The second advantage is that it is computationally much cheaper to include the effects of interstitial gas in a corotating frame of reference. Note that for a large scientific community usage of a corotating frame of reference is standard and common practice, for example, in the meteorological and the fluid dynamics community.[40]

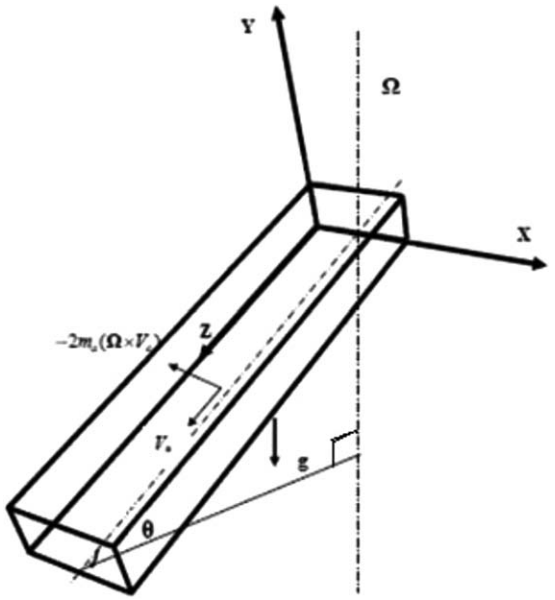

Figure 2. Definition of axes and orientation of gravitational and Coriolis forces experienced by particles flowing down a rotating inclined chute in our discrete particle model.

When working in a corotating frame of reference, pseudoforces arise due to the noninertial motion of the system. Every individual particle a in the rotating system experiences an additional Coriolis force and centrifugal force, both of which must be added to the equation of motion Eq. 1

$$(\mathbf{F})_{\mathrm{rotating}} = (\mathbf{F})_{\mathrm{stationary}} - 2m_a(\boldsymbol{\Omega}\times\mathbf{v}_a) - m_a(\boldsymbol{\Omega}\times[\boldsymbol{\Omega}\times\mathbf{r}_a]) \tag{13}$$

where $\boldsymbol{\Omega}$ is the angular velocity of the chute and $\mathbf{r}_a$ the position of particle a relative to a position located on the axis of rotation. The rotation axis and the directions of the Coriolis and centrifugal accelerations are all shown in Figure 2.

Similarly, every particle will experience an additional Coriolis torque, which must be added to Eq. 2

$$(\mathbf{T})_{\mathrm{rotating}} = (\mathbf{T})_{\mathrm{stationary}} - I_a(\boldsymbol{\Omega}\times\boldsymbol{\omega}_a) \tag{14}$$

Inclusion of a Coriolis torque is necessary because, even when no other torques apply to a particle, in the comoving frame of reference the direction of the particle's angular momentum will appear to reorient. When applying Eq. 14, this reorientation is such that the true angular momentum (i.e., when viewed from an outside inertial system) is exactly conserved.

We emphasize that the physics does not change when going from an inertial to a corotating frame of reference. The contact forces, which depend on relative positions and relative velocities, remain unaffected. When focusing only on flow through a rotating chute, as we do in this work, the use of pseudoforces is simpler than including interactions between particles and an explicitly moving wall. When the

nonrotating process equipment before or after the chute is also modeled, the advantage of using a corotating frame disappears, and using an inertial frame is preferred.

Equations for gas hydrodynamics

In this work, we will test the role of interstitial gas for both nonrotating and rotating chute. The motion of the gas phase is described by the equations of mass and momentum conservation. Given the large number of particles in DEM simulations one usually resorts to the volume-averaged Navier–Stokes equations. From mass conservation, we have

$$\frac{\partial(\varepsilon\rho_g)}{\partial t}+\nabla\cdot(\varepsilon\rho_g\mathbf{u})=0 \tag{15}$$

where ρ_g is the gas density, ε is the local porosity, and $\mathbf{u}$ is the gas velocity measured in the corotating frame. The momentum equation for the gas phase reads

$$\frac{\partial(\varepsilon\rho_g\mathbf{u})}{\partial t}+\nabla\cdot(\varepsilon\rho_g\mathbf{u}\mathbf{u})=-2\varepsilon\rho_g\boldsymbol{\Omega}\times\mathbf{u}-2\varepsilon\rho_g\boldsymbol{\Omega}\times(\boldsymbol{\Omega}\times\mathbf{r}) -\varepsilon\nabla p-\mathbf{S}_p-\nabla\cdot(\varepsilon\boldsymbol{\tau}_g)+\varepsilon\rho_g\mathbf{g} \tag{16}$$

where p is the gas pressure, $\mathbf{S}_p$ is a source term caused by drag with the particles (see later) and $\mathbf{g}$ is the gravitational acceleration. Note that the first two terms on the right-hand side of Eq. 16 take into account the effect of system rotation on vectorial quantities (in this case velocities),[41] but that no such terms appear in the continuity equation Eq. 15 because mass is a scalar quantity. The viscous stress tensor for the gas phase is assumed to obey the general form for a Newtonian fluid, that is

$$\boldsymbol{\tau}_g=-(\lambda_g-\frac{2}{3}\mu_g)(\nabla\cdot\mathbf{u})\mathbf{I}-\mu_g(\nabla\mathbf{u}+(\nabla\mathbf{u})^T) \tag{17}$$

where λ_g is the gas-phase bulk viscosity, μ_g is the gas-phase shear viscosity, and $\mathbf{I}$ the unit tensor.

To solve the above equations, the chute is divided into NX $\times$ NY $\times$ NZ computational cells (in the corotating frame of reference). The pressure and gas velocity in each cell can be calculated from discretized versions of Eqs. 15 and 16.[42]

The sink term $\mathbf{S}_p$ in Eq. 16 represents the drag experienced by the particles in the computational cell, which we treat as point sources of momentum for the gas phase. In detail[42]

$$\mathbf{S}_p=\frac{1}{V}\int\sum_{a=1}^{N\text{part}}\frac{\beta V_a}{1-\varepsilon}(\mathbf{u}-\mathbf{v}_a)\delta(\mathbf{r}-\mathbf{r}_a)dV \tag{18}$$

where V represents the local volume of the computational cell and V_a is the volume of particle a. The distribution function δ distributes the reaction force acting on the gas phase to the computational cells, where a trilinear interpolation method is used in this work.[18] The interphase momentum transfer coefficient, β, describes the drag of the gas phase acting on the particles, which is modeled using the correlation proposed by Beetstra[43]

$$\begin{aligned}\beta&=A\frac{(1-\varepsilon)^2}{\varepsilon}\frac{\mu_g}{d_a^2}+B\ (1-\varepsilon)\mathrm{Re}\\ A&=180+\frac{18\varepsilon^4}{1-\varepsilon}\left(1+1.5\sqrt{1-\varepsilon}\right)\\ B&=\frac{0.31(\varepsilon^{-1}+3\varepsilon(1-\varepsilon)+8.4\mathrm{Re}^{-0.343})}{1+10^{3(1-\varepsilon)}\mathrm{Re}^{2\varepsilon-2.5}}\end{aligned} \tag{19}$$

where $\mathrm{Re}=\varepsilon\rho_g|\mathbf{u}-\mathbf{v}_a|d_a/\mu_g$ is the particle Reynolds number and $d_a=2R_a$ is the particle diameter.

The pressure and drag forces acting on the particles in Eq. 1 are given by

$$\mathbf{F}_a^p=-V_a\nabla p \tag{20}$$

$$\mathbf{F}_a^d=\frac{V_a\beta}{1-\varepsilon}(\mathbf{u}-\mathbf{v}_a) \tag{21}$$

Note that total momentum of the gas and solid phase is locally conserved: Eq. 20 is consistent with the third term on the r.h.s. of Eq. 16, and Eq. 21 balances the source term in Eq. 18.

The boundary conditions for the gas phase imposed for the side walls and the bottom wall of the chute is no-slip and for the top boundary we impose a prescribed velocity in all three directions equal to $\mathbf{u}=-\boldsymbol{\Omega}\times(\mathbf{r}-\mathbf{r}_{\text{axis}})$, representing the position-dependent cross-wind (lid-flow) present at the open chute top during the experiments. We emphasize that the latter boundary condition represents a worst-case scenario for the influence of the gas because (1) with respect to gas flow in the width-wise direction, we assume a maximum amount of lid-driven flow, while in reality the air near the open top boundary of the chute will not remain stagnant in the inertial lab-frame and (2) because with respect to the gas flow in the streamwise direction, we assume a maximum amount of deceleration caused by the top boundary (near-zero z-velocity) instead of a stress-free condition (with zero velocity gradient). A coflow velocity inlet boundary condition is imposed at the inlet and a constant pressure outlet boundary condition at the exit of the chute.

Simulation settings

The physical properties of the spherical glass particles and the conditions for the simulation are shown in Table 1. The flow domain was divided into small cells, with the size of each cell approximately twice the particle diameter. This cell size has been shown to yield accurate results for the particle-gas interaction forces in simulations of dense fluidized beds.[44]

In our DEM simulations, the chute is initially empty, as is the case in the physical experiments. Simulations are carried out for a constant mass flow rate at the inlet of the chute. We introduce the particles at the chute entrance in a rectangular area with a variable height, which we refer to as the sluice height. We arrange the particles in a bcc-lattice using as many particles as can be fitted in the sluice height. Because the mass rate is fixed, the streamwise velocity with which the new particles are initialized is smaller when the sluice height is larger. Specifically, we introduce the particles with a mass flow rate of 1.6 kg/s, which is equal to the mass flow rate of our previous experiments.[36] The total number of particles in the chute depends on the inclination angle and rotation rate and also fluctuates in time. The typical number was approximately 31,000 for an inclination angle of 30° and approximately 26,000 for 40°. The simulations were carried out on a single core of an Intel Xeon E5520 processor (at 2.27 GHz). In general, each simulation required 60 h of calculation time for each 6 s of simulation.

Computational Measurements

Calculation of bed height in simulations

We calculated the bed height similarly in simulations and experiments.[36] In the experiments, an electronic height sensor was used which measures the height by averaging the

Table 1. Simulation Settings for Monodisperse Flow of Glass Particles

1	Channel	Dimensions: Width = 0.08 m, Depth = 0.045 m, Length = 0.9 m	Number of computational cells: NX = 16 NY = 15 NZ = 150
2	Particles	Diameter = 3 mm Total number of particles (typical) = 26,000–31,000 Density = 2550 kg/m^3 Mass flow rate = 1.6 kg/s	
3	Collision parameters	Particle–particle collisions Normal spring stiffness Coefficient of normal restitution Coefficient of tangential restitution Coefficient of friction Coefficient of rolling friction Particle-wall collisions Coefficient of normal restitution Coefficient of tangential restitution Coefficient of friction Coefficient of rolling friction	 k_n = 1000 N/m $e_{n,\ pp}$ = 0.97 $e_{t,pp}$ = 0.33 μ_{pp} = 0.12 $\mu_{r,pp}$ = 0.0 $e_{n,pw}$ = 0.95 $e_{t,pw}$ = 0.33 μ_{pw} = 0.22 $\mu_{r,pw}$ = 0.0
4	Time and time step	Total simulation time Time step	T = 6.0 s dt = 2.5 × 10^{-6} s

top of the highest particles over a circular area with a diameter of 28 mm. Independent measurements on stationary packed beds showed that the experimental error in these bed height measurements is about 50% of a particle diameter, that is, 1.5 mm. We measured the averaged bed height at three different width-wise positions, that is, the left, center, and right side of the chute, centered at 0.015, 0.045, and 0.065 m of the 0.08-m wide chute. In our simulation, the time averaged bed height was calculated over a matrix of 5 × 5 cells with similar dimensions as the sensor surface, as shown in Figure 3.

Calculation of surface velocity in simulations

In our previous experiments,[36] we used PIV to determine the average two-dimensional (2-D) velocity field of the visible surface particles.[45,46] The basic principle of PIV is to record two images with a short time delay and determine the displacement of the particles between the two images with a spatial cross-correlation algorithm on two consecutive images. Careful selection of the time between two consecutive images was required to minimize the influence of out-of plane motion of particles. We set the resolution and magnification in such a way that the particle images are about 5 pixels in diameter, which is known to give accurate results in PIV measurements.[46,47] A multipass algorithm was used with an initial interrogation area size of 32×32 pixels and a final size of 16×16 pixels nonoverlapping interrogation areas, which yields an approximated displacement error of O(0.1) pixels.[46] Due to the very high seeding density (particles per interrogation area), there were practically no outliers. Any remaining outliers were removed with a standard median filter. After postprocessing, a time-averaged velocity field was obtained from a sequence of instantaneous velocity fields obtained over a time interval during which the flow was steady. We found that the error in this velocity field is 0.2%, which is relatively small. Full details and results are given in Shirsath et al.[36]

In this work, we will validate our DEM simulations by comparing particle velocity measurements between experiments and simulations. To enable a direct comparison, the 2-D particle velocity field is calculated for those particles that are optically visible from above the chute, because in the experiments the camera was mounted perpendicularly above the chute at a large distance of 1.5 m. In our simulations,

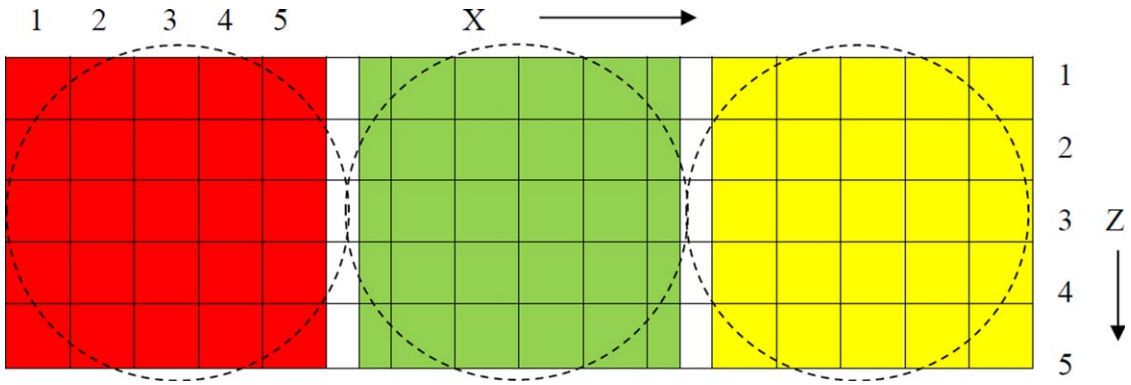

Figure 3. Top view of a section of the chute with the grid cell structure used for bed height calculation.

Chute walls are present at the left and right side of this figure and the granular flow is in the *Z* direction. In the experiments, the bed height is averaged over a circular area at three width-wise positions: left, center, and right (dashed circles). For validation, in our simulations the bed height is averaged over approximately the same areas consisting of 5 × 5 cells, indicated by red, green, and yellow color, respectively. [Color figure can be viewed in the online issue, which is available at wileyonlinelibrary.com.]

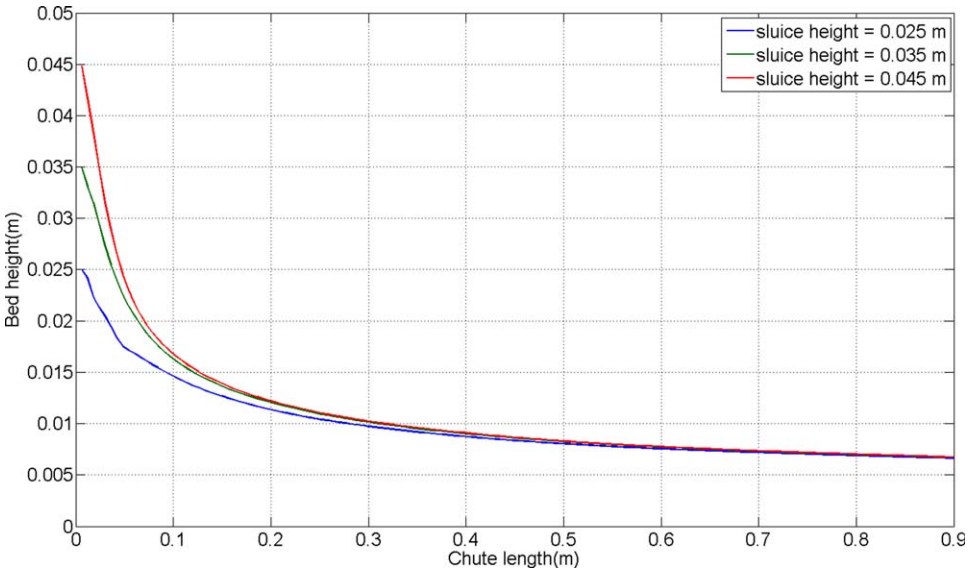

Figure 4. Time-averaged bed height along the length of the chute inclined at 30° for different sluice heights feeding a nonrotating chute.

The particle mass loading rate is constant and equal to 1.6 kg/s. In all subsequent figures a sluice height of 0.045 m is used, and the origin of the horizontal axis is shifted to obtain a match between experiment and simulation in a single point, as described in the main text. [Color figure can be viewed in the online issue, which is available at wileyonlinelibrary.com.]

the surface velocity is calculated by time-averaging the average velocity of the topmost six particles in each streamwise and with spanwise cell. This choice closely matches the number of experimentally visible particles because at the given particle diameter of 3 mm, and the width-wise and length-wise size of the cells of 5×6 mm^2, it is expected that 4–6 particles will be visible from above the chute. We have checked the dependence of the surface velocity measurements on the number of topmost particles used, and found only a negligible influence (less than 0.1% difference in measured surface particle velocity) for particle numbers ranging from 3 to 12.

Results and Discussion

In this section, results obtained from the DEM simulations are compared with the experimental results of Shirsath et al.[36] Specifically, we will focus on the particle bed height and streamwise and spanwise particle velocities at the surface of the granular flow for different rotation rates and fixed angles of inclination of 30° and 40°. First, the effect of charging at the inlet of the chute, and subsequently the influence of the interstitial gas on the granular flow behavior is studied. We then report on a sensitivity study to check the effect of the particle collision parameters on particle bed height in the chute.

Influence of inlet particle charging

In real-life blast furnace processing, the particles are charged from a hopper onto the surface of the chute. In our simulations, we can pour the particles in a similar way. However, we expect that the granular flow through the chute is primarily determined by the particle properties and the particle mass loading rate. In other words, we expect that memory of the details with which the particles are introduced into the chute will fade quickly relative to the time needed to flow down the chute. To confirm this, we introduce the particles at the inlet of the chute in a rectangular area with a variable height which we refer to as the sluice height. We arrange the particles in a bcc-lattice using as many particles as can be fitted in the sluice height. Because the mass rate is fixed (to 1.6 kg/s), the streamwise velocity with which the new particles are initialized is smaller when the sluice height is larger. We performed several sets of simulations for different sluice heights feeding a nonrotating chute, as shown in Figure 4. Figure 4 shows that the bed height is indeed independent of the sluice height (and therefore, independent of initial velocity) after approximately 0.2 m from the inlet of the chute, especially when the sluice height is more than 3 cm. The same holds true for the particle velocity. We have also tested the influence of sluice height for an inclination angle of 40° and for rotating chutes, rotating at the maximum rate of 16 rpm. Moreover, we performed a series of simulations where the particles are introduced in the same manner as in the experiments, that is, from a hopper at the top directly onto the chute surface (which are computationally more expensive simulations). For all these cases we found that, again, the bed height and particle velocity are independent of sluice height after approximately 0.2 m from the inlet (not shown). In all subsequent simulations, we have used a constant sluice height of 0.045 m.

Conversely, the bed height and surface flow velocity do depend on the manner of particle introduction in the first 0.2 m of the simulated chute. To be able to compare experiments and simulations, we have determined the first point at which the bed height and surface flow velocity match between experiment and simulation for a single nonrotating chute at an angle of inclination of 30°. In all subsequent figures, we have shifted the origin (for distance along the flow direction) to this point. It is important to have exactly the same distance to the rotation axis in both simulations and experiments. In detail, in both our simulations and in our experiments the axis of rotation is cutting through the bottom plane at a distance of 0.035 m before the point of origin determined above.

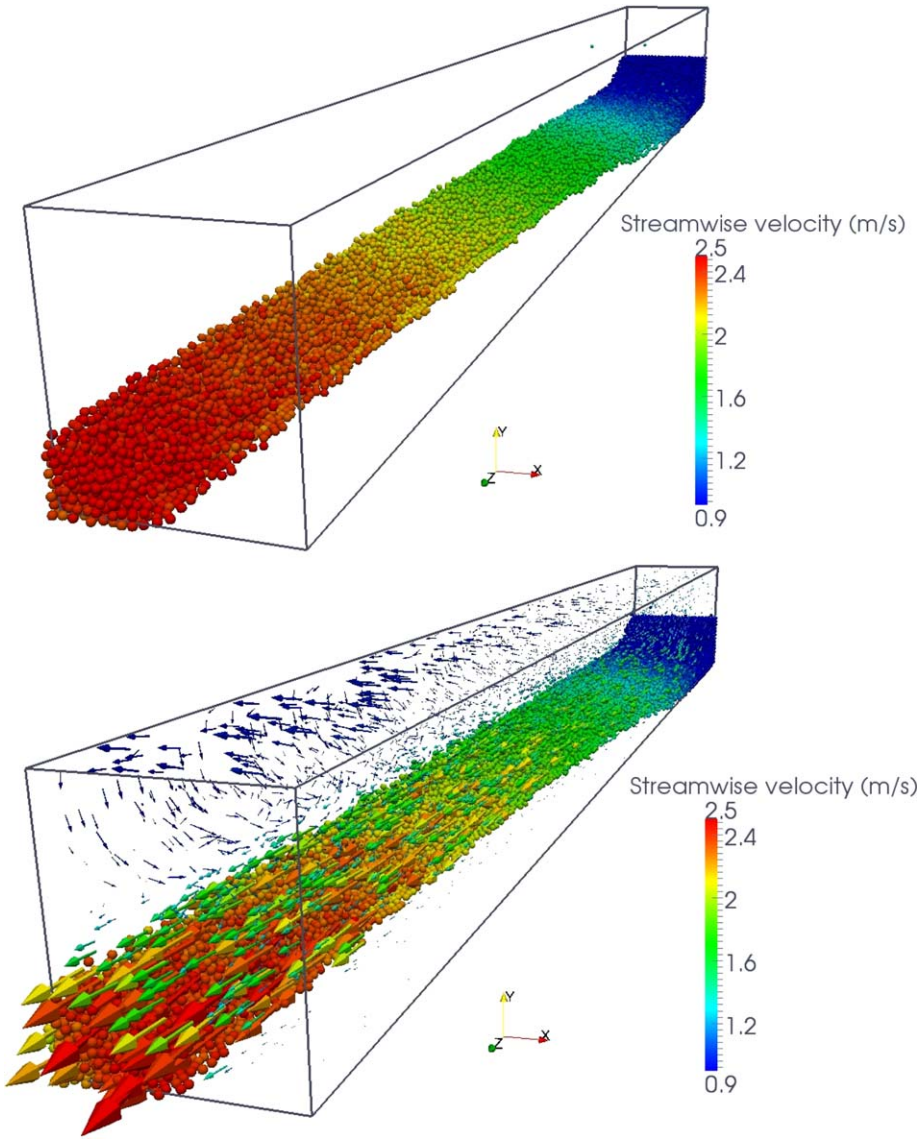

Figure 5. Snapshots of steady-state granular flows, flowing from top to bottom through a chute inclined at 30° and rotating at 16 rpm.

Particles are color-coded by their velocity. Top: flow without gas drag. Bottom: flow with gas drag included in the simulation; arrows show the gas velocity vectors above the particle bed. [Color figure can be viewed in the online issue, which is available at wileyonlinelibrary.com.]

Influence of interstitial gas

A granular material flow is defined as the flow of a fluid-particle system in which the effects of the interstitial fluid are assumed to be negligible. This is the asymptotic state of particle-fluid flows in which the majority of the momentum is transferred by particle–particle interactions. Intuitively this implies that: (1) the fluid viscosity is low, minimizing the effect of viscous drag on the particles and (2) that the solid density is much higher than the fluid density, so minimizing both relative buoyancy (gas–solid) and added mass effects. To study the influence of the interstitial gas for our system, we performed simulations with and without gas. In the simulations with gas, both the particles and the gas are introduced at a constant flow rate. Figure 5 shows snapshots of monodisperse flows down chute with and without gas for rotating case (16 rpm). Figure 6 shows the average particle velocity in both a nonrotating chute (0 rpm) and a rotating chute (16 rpm), which increases from a low value at the inlet to a large value at the outlet as a result of gravity. When gas is included in the simulation, the averaged velocity decreases slightly in both the nonrotating and the rotating chute. However, the influence of the interstitial air is relatively minor, lowering the velocity at the end of the chute by 2–3% in a nonrotating chute and 5–10% in a rotating chute (at both angles of inclination studied in this work). We will show in the remaining part of this work that this small effect can effectively and efficiently be incorporated by tuning the coefficient of friction, leading to an accurate agreement with experimentally observed particle velocities and bed height.

Sensitivity study of collision parameters

To investigate the sensitivity of the flow on the collisional properties of the particles, we have performed a series of DEM simulations in which the collisional parameters were

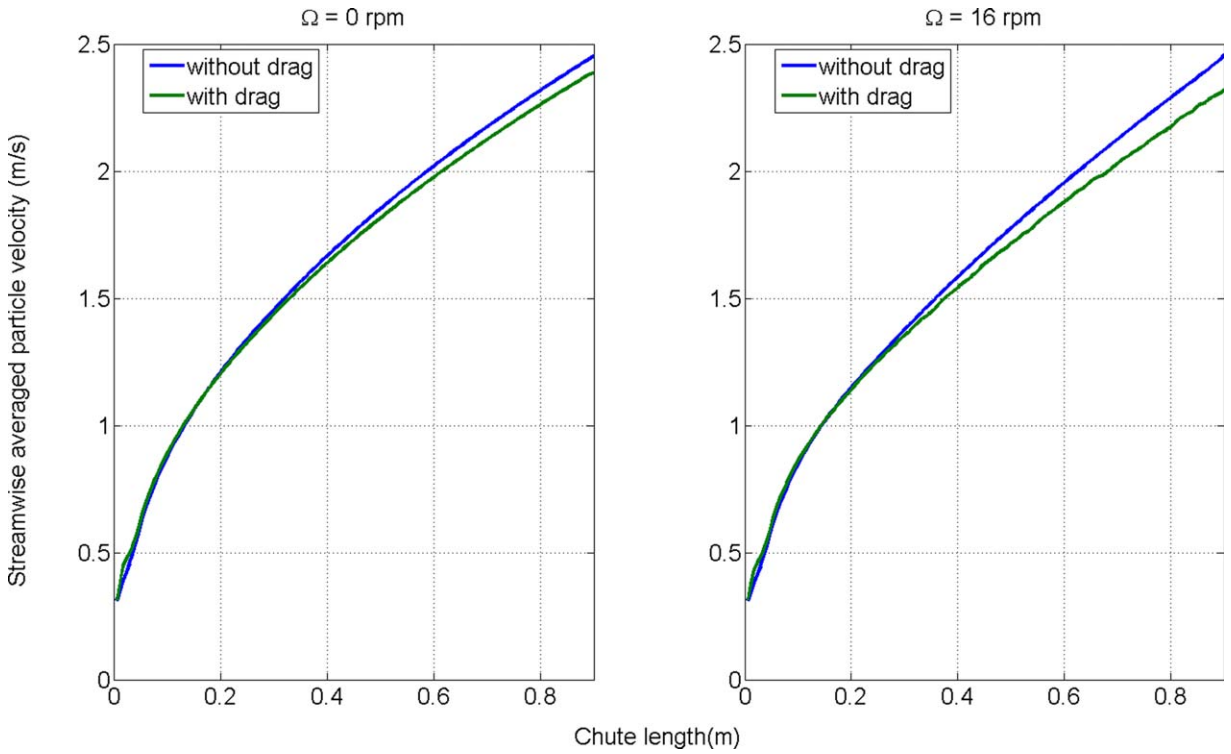

Figure 6. Time-averaged streamwise particle velocity in a chute inclined at 30°, comparing simulations with and without air drag.

[Color figure can be viewed in the online issue, which is available at wileyonlinelibrary.com.]

systematically varied from the base case (for glass particles) given in Table 1. Each time one particle–particle collision parameter was varied and its influence on the surface velocity of the particles was determined.

Base Case Simulation: Glass Particles. The base case simulation was performed for the flow of monodisperse glass spheres down a chute inclined at 30°. We note that at first we used in our simulations the coefficient of friction between glass particles and between glass particles and plexiglass walls as measured by single particle experiments in our lab. We found that the coefficient of friction between glass particles is 0.1189 and between glass particle and plexiglass wall is 0.097. These values are close to the values reported in the literature.[48] Similar to findings in the literature,[42] we found that we actually needed to use a higher value for the friction coefficient between particle and wall (0.22 instead of 0.097) to obtain quantitative agreement with the experimental (nonrotating) chute flow results. This higher value is compensating for the fact that smaller values of the materials' Young's modulus (lower effective spring stiffnesses) are used in the simulations to allow for reasonable time integration steps. To be precise: in our work, the value for the particle-wall friction coefficient has been tuned once to achieve maximum agreement between the simulated and experimental surface velocity and bed height for the nonrotating base case at 30° chute angle. All other cases are then used as validation of our model.

The surface velocity of the particles obtained from the base-case simulation is compared with the experimental surface velocity in Figure 7. We observe that the simulated time-averaged surface velocity is in good agreement with the experimental surface velocity at the same operating conditions.

Effect of Tangential Restitution Coefficient. We first study the influence of the coefficient of tangential restitution (for particle–particle and particle-wall collisions) on the averaged surface velocity in the chute. We varied the tangential restitution coefficient e_t from 0.1 to 0.9, where the base case value is 0.33, while keeping $e_{t,pw}$ equal to e_t. In all cases, we obtained results which are nearly indistinguishable from the base case shown in Figure 7 (and are, therefore, not shown). This is already a first indication that in our systems the tangential forces between the particles are usually saturated to values limited by the coefficient of friction. We will return to this point when we investigate the influence of the coefficient of friction.

Effect of Normal Restitution Coefficient. Next, we study the influence of the coefficient of normal restitution for both particle–particle and particle-wall collisions. We varied e_n from 0.3 to 0.99, where 0.97 is the base case, while keeping the ratio $e_{n,pw}/e_{n,pp}$ constant. Under certain conditions the coefficient of normal restitution is a sensitive parameter for the flow behavior in DEM studies.[49,50] However, for chute flow we find only a very weak dependence of the average velocity on e_n (not shown). This is in contrast with, for example, the flow of particles in a fluidized bed, where small perturbations in solid fraction grow exponentially, reinforced by the gas flow and inelastic collisions. Such a formation of heterogeneous structures does not occur in the chute flows studied here.

Effect of Coefficient of Friction. The coefficient of friction μ is important because it determines the maximum tangential force that can be exerted at the surface of a particle for a given amount of normal force. As such, it determines the transition from a sticking to a sliding collision. We

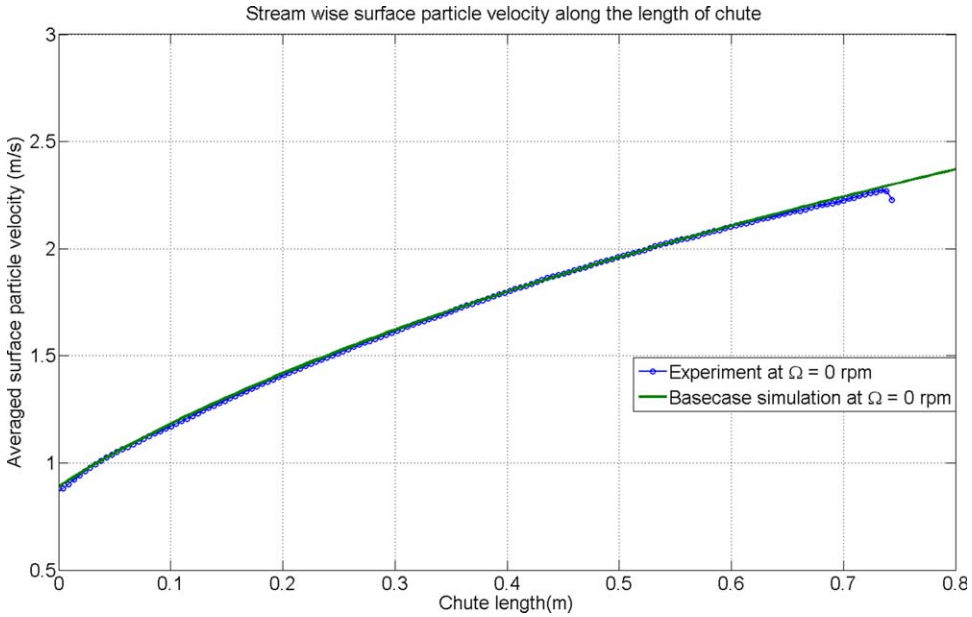

Figure 7. Time-averaged streamwise surface particle velocity along the length of the chute inclined at 30°.

Base case simulation for the collision properties of glass spheres. Small circles represent experimental data and the line is from the base case simulation. [Color figure can be viewed in the online issue, which is available at wileyonlinelibrary.com.]

performed several simulations using different values of the coefficient of friction, with a fixed ratio for particle-wall collisions, while keeping all other collision parameters constant. The result presented in Figure 8 shows that the streamwise surface particle velocity is very sensitive of the value of the coefficient of friction. With increasing μ, the surface velocity decreases continuously. From this, we conclude that the particles are exerting relatively large tangential forces on each other and are considerably slowed down if their surfaces are rough. The transition between sticking and sliding collisions, determined by the coefficient of friction, is therefore one of the most important phenomena in particle chute flow.

Effect of Coefficient of Rolling Friction. Finally, we study the effect of the coefficient of rolling friction μ_r (for both particle–particle and particle-wall collisions) on the particle surface velocity in the chute. The value of the rolling friction was varied between zero and its maximum which can be reasonably assumed for near-spherical particles, that is, a maximum equal to the coefficient of friction μ, while keeping all other parameters constant as shown in Table 1. Figure 9 shows that the influence of the coefficient of rolling

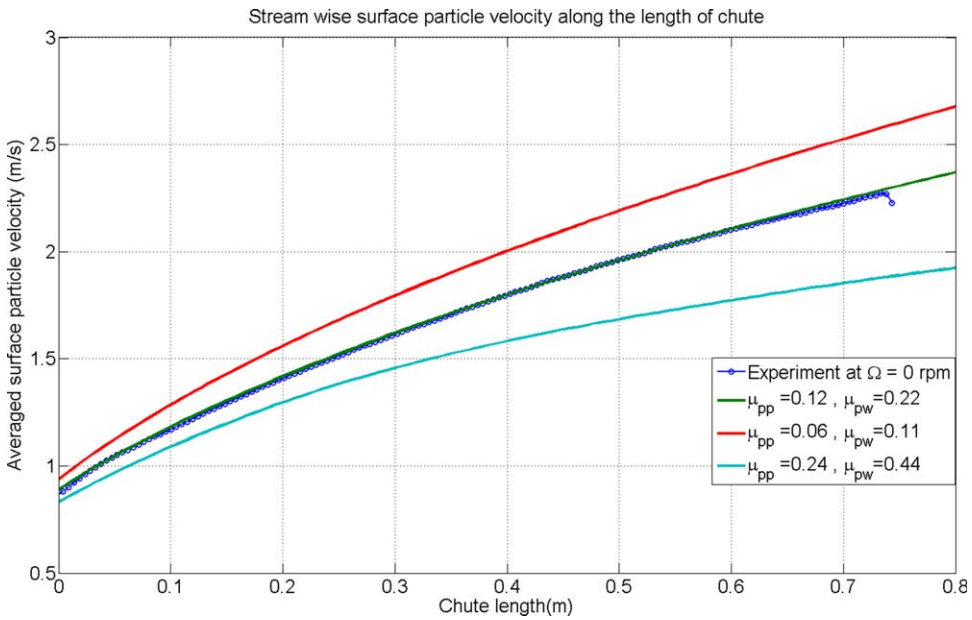

Figure 8. Time-averaged streamwise surface particle velocity along the length of chute inclined at 30° for different coefficients of friction.

Small circles are experiments using glass and lines are simulations (where the green line is the base case for glass). [Color figure can be viewed in the online issue, which is available at wileyonlinelibrary.com.]

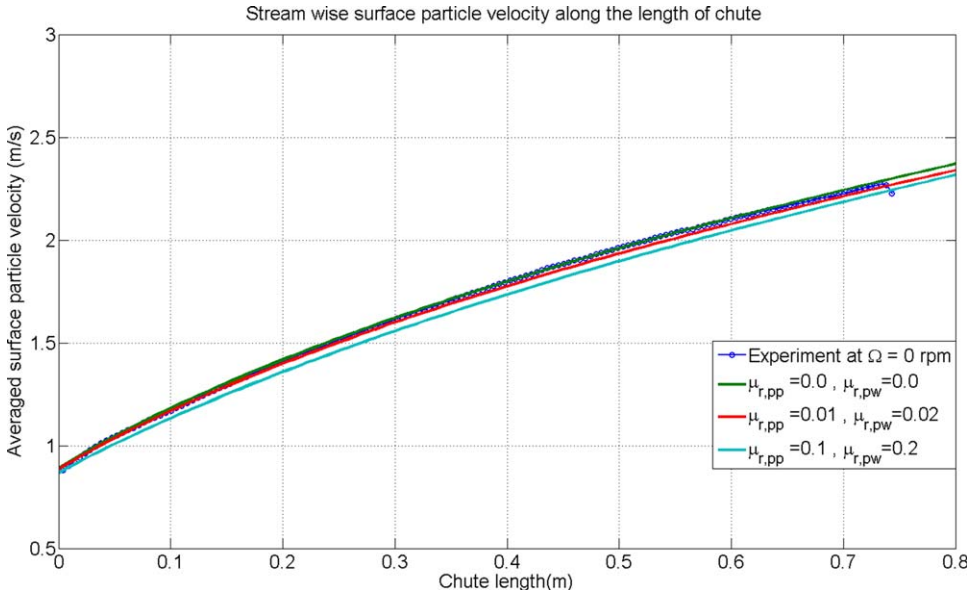

Figure 9. Time-averaged streamwise surface particle velocity along the length of chute inclined at 30° for different coefficients of rolling friction.

Small circles are experiments on glass and lines are simulations (the green line is the base case for perfect glass spheres). [Color figure can be viewed in the online issue, which is available at wileyonlinelibrary.com.]

friction on the surface particle velocity is relatively minor, except when it is close to the coefficient of friction. With increasing rolling friction, the surface velocity decreases slightly, except in the initial part of the chute where the particles do not yet rotate significantly, and are therefore not yet influenced by rolling friction.

Summary of Sensitivity Study. In summary, for the type of granular chute flow considered here, we have found that the streamwise surface particle velocity is very sensitive to the value of the coefficient of friction, somewhat sensitive to the value of the coefficient of rolling friction, and insensitive to the values of the coefficients of normal and tangential restitution. It is, therefore, most important to choose the coefficients of friction between particles and between particles and walls correctly. The right choice can only truly be confirmed by comparing simulation predictions with experiments for a range of properties and a range of experimental conditions, which is the topic of the next section.

Validation: Comparison with Experimental Results

In the previous section, we have confirmed that our DEM simulations are able to predict the steady-state streamwise surface particle velocity of an experimental system consisting of glass spheres of 3 mm flowing down a nonrotating chute inclined at 30°. The reader is reminded that the parameters for this base case are given in Table 1. In the remainder of this article, we validate the model for more chute settings, with chutes rotating at different rotation rates and two different inclination angles, comparing not only the streamwise surface particle velocity, but also the spanwise surface particle velocity and particle bed height profile.

The major effect of chute rotation is a sideways deflection of the particle stream due to Coriolis forces present in the frame of reference corotating with the chute. This is confirmed in Figure 10, which shows snapshots of the steady-state flow of monodisperse particles in a chute inclined at 30° for different rotation rates, where colors indicate the magnitude of the velocity of the particles.

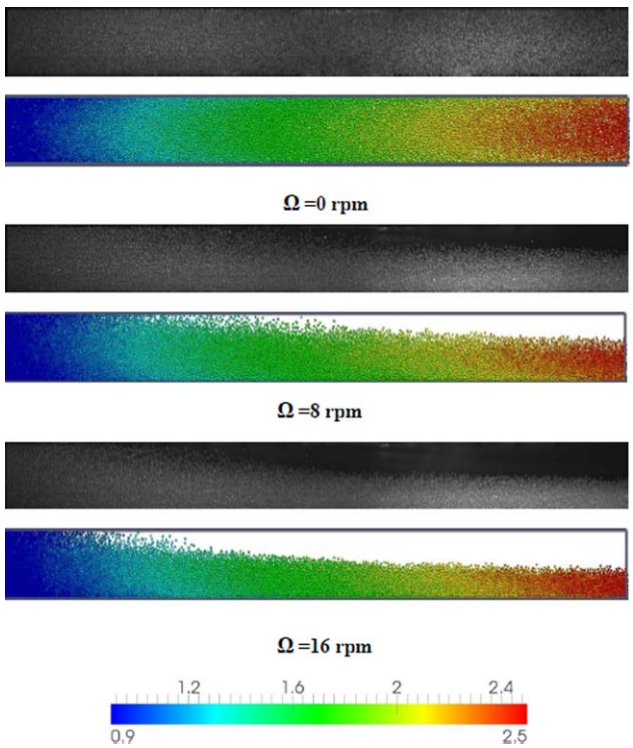

Figure 10. Top view snapshots of steady-state granular flows, flowing from left to right through a chute inclined at 30°.

The chute is rotating with a rotation rate of 0, 8, or 16 rpm. Gray scale: experiments. In the simulations snapshots, particles are color-coded according to the magnitude of their streamwise velocity, from blue to red for low to high velocity. [Color figure can be viewed in the online issue, which is available at wileyonlinelibrary.com.]

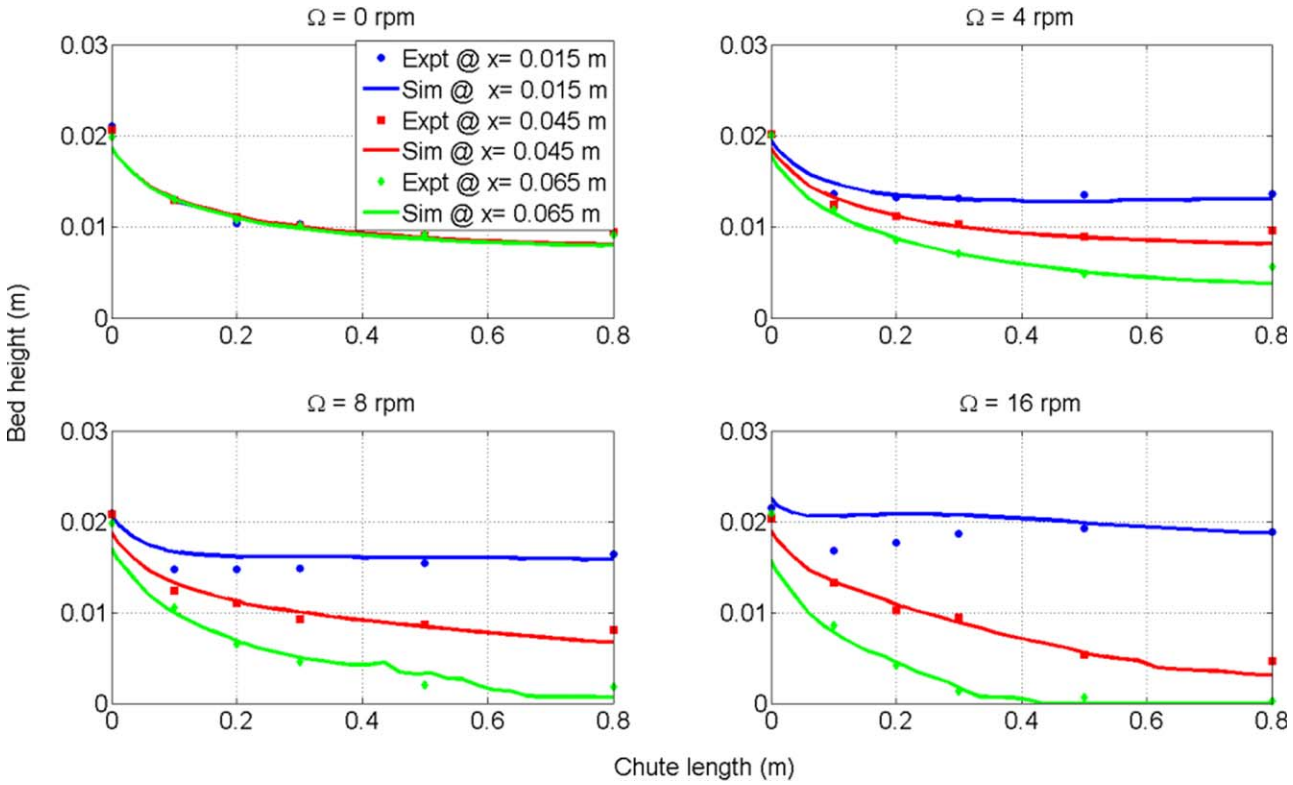

Figure 11. Bed height as a function of streamwise position (along the length of the chute) for three different widthwise positions in a chute inclined at 30°, rotating with rates of 0, 4, 8, and 16 rpm.

Small circles are experiments and lines are simulations. Note that the bed height is averaged over an area equal to the height sensor surface area. [Color figure can be viewed in the online issue, which is available at wileyonlinelibrary.com.]

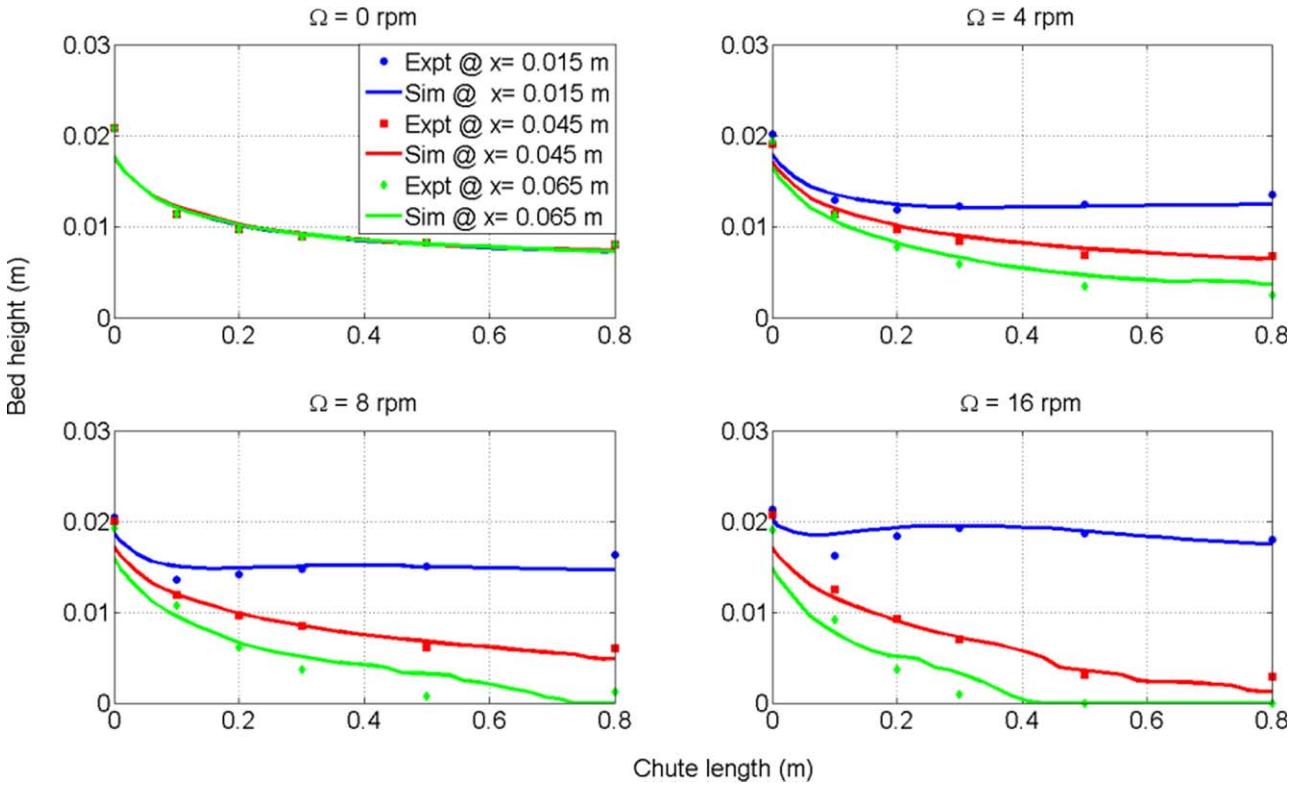

Figure 12. Bed height as a function of streamwise position (along the length of the chute) for three different widthwise positions in a chute inclined at 40°, rotating with rates of 0, 4, 8, and 16 rpm.

Small circles are experiments and lines are simulations. Note that the bed height is averaged over an area equal to the height sensor surface area. [Color figure can be viewed in the online issue, which is available at wileyonlinelibrary.com.]

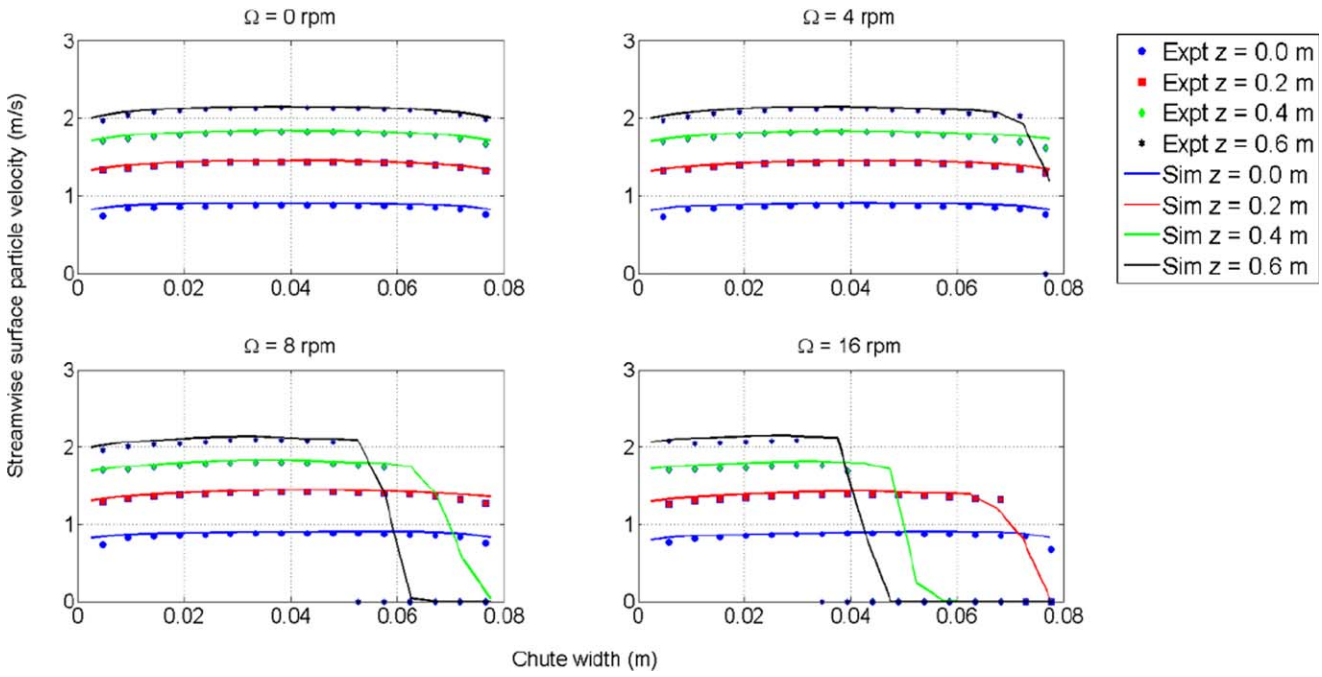

Figure 13. Streamwise particle velocity along the width of the chute inclined at 30° for a rotation rate of 0, 4, 8, and 16 rpm.

Symbols represent the experiments, lines are results for simulations. [Color figure can be viewed in the online issue, which is available at wileyonlinelibrary.com.]

Particle bed height

Figure 11 shows the bed height as a function of position along the length of the chute, for a chute inclined at a fixed angle of 30°. Figure 12 shows the same measurements for an inclination angle of 40°. The bed height is averaged over an area corresponding to the area of the ultrasonic height sensor. The simulation results (lines) are compared with experimental results (symbols) for three different width-wise positions in the chute and six different length-wise positions. For the nonrotating chute, the bed height continuously decreases along the length of chute, and the results are nearly indistinguishable for the different width-wise positions. As the rotation rate of the chute increases, the bed height increases on the right side of the chute and

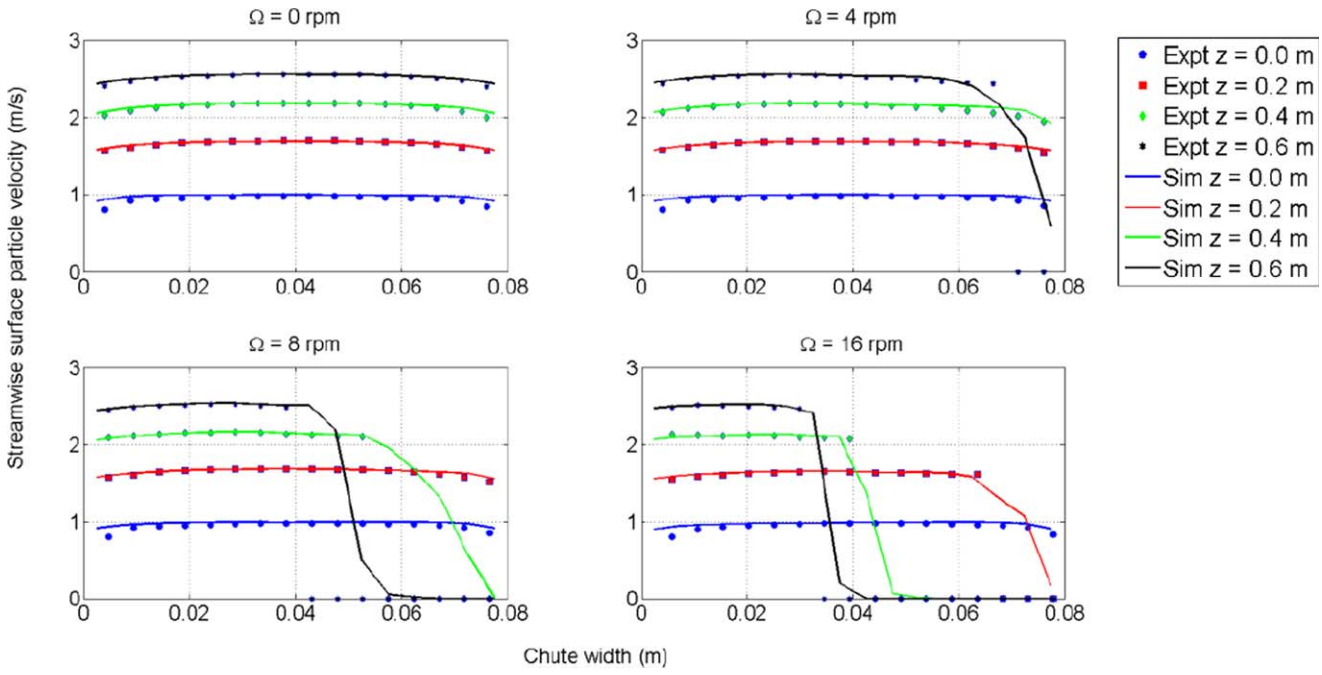

Figure 14. Streamwise particle velocity along the width of the chute inclined at 40° for a rotation rate of 0, 4, 8, and 16 rpm.

Symbols represent the experiments, lines are results for simulations. [Color figure can be viewed in the online issue, which is available at wileyonlinelibrary.com.]

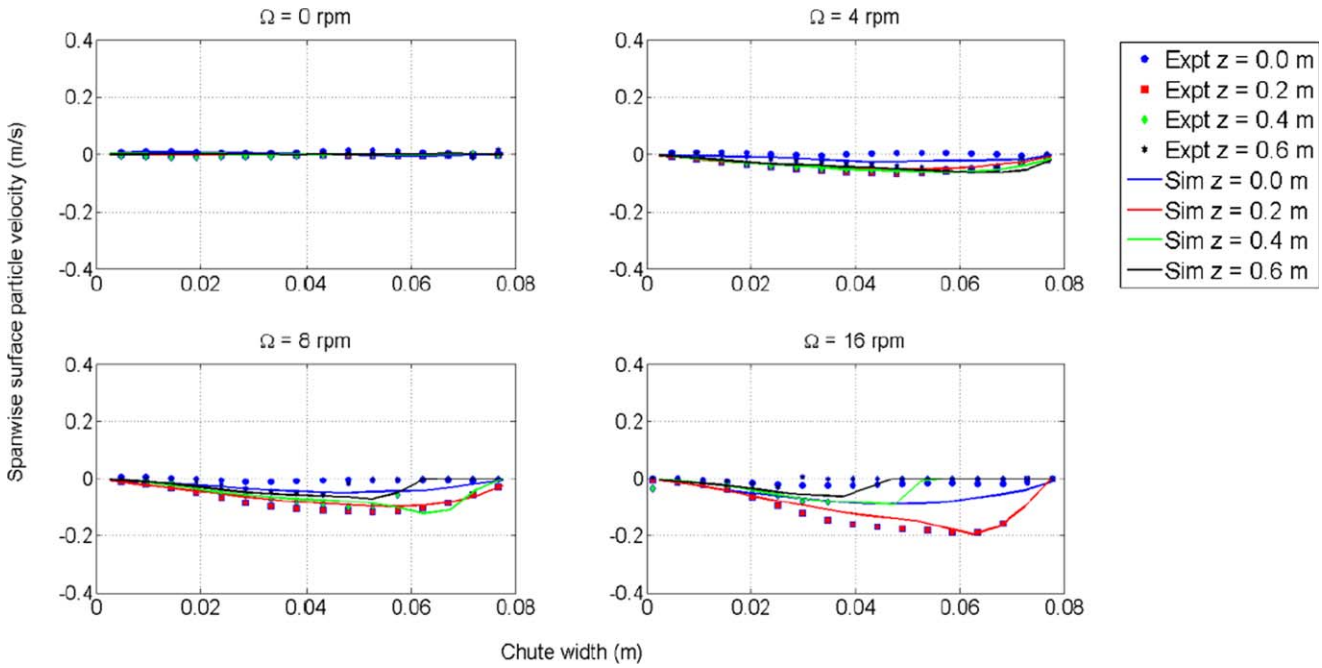

Figure 15. Spanwise particle velocity along the width of chute for an inclination angle of 30° for a rotation rate of 0, 4, 8, and 16 rpm.

Symbols represent the experiments, lines are results from simulations. [Color figure can be viewed in the online issue, which is available at wileyonlinelibrary.com.]

decreases on the left side. Generally, given the experimental error of approximately 1.5 mm, the simulation results are in good agreement with the experimental measurements. There is one exception: at higher rotation rates of 8 and 16 rpm, the experiments show a maximum in the height as a function of streamwise position at the right side of the chute (blue symbols), which is much less apparent in our simulations (blue lines). We attribute this to our previous observation that the precise manner of particle introduction is important for the first 0.2 m. At the highest rotation rate of 16 rpm, memory of the precise manner of introduction appears to extend somewhat further down the chute, but agreement between experiments and simulations is found again beyond 0.4 m.

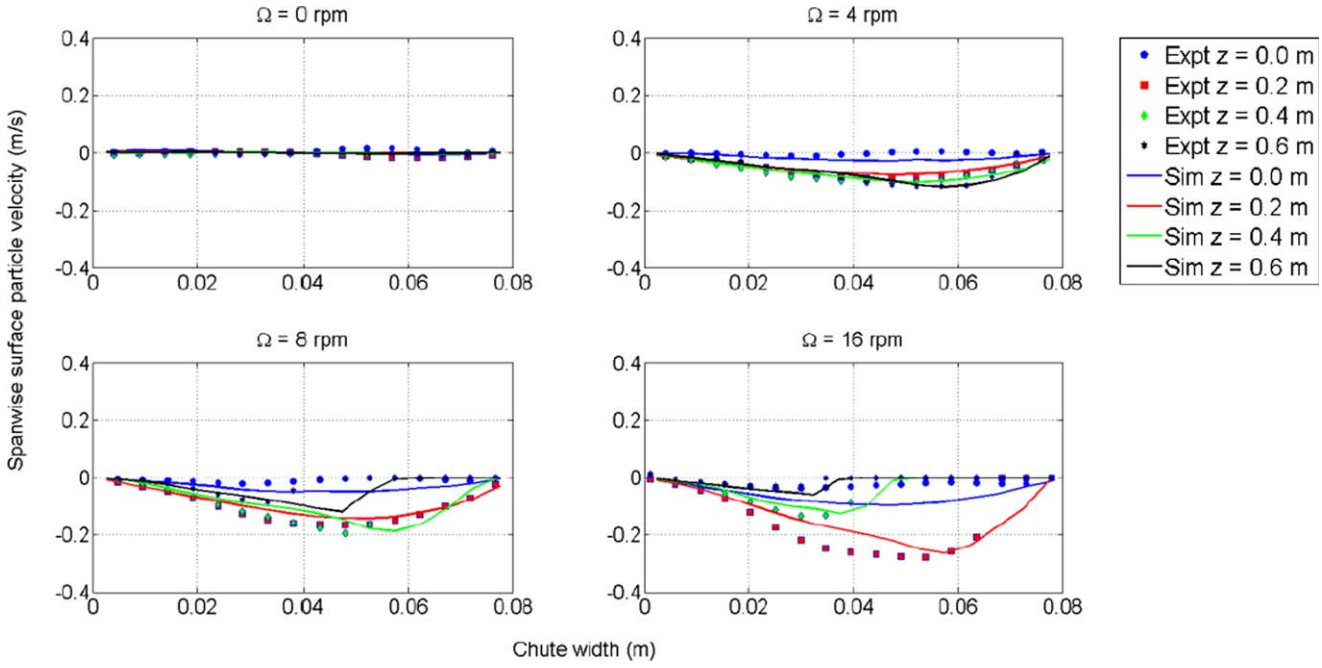

Figure 16. Spanwise particle velocity along the width of chute for an inclination angle of 40° for a rotation rate of 0, 4, 8, and 16 rpm.

Symbols represent the experiments, lines are results for simulations. [Color figure can be viewed in the online issue, which is available at wileyonlinelibrary.com.]

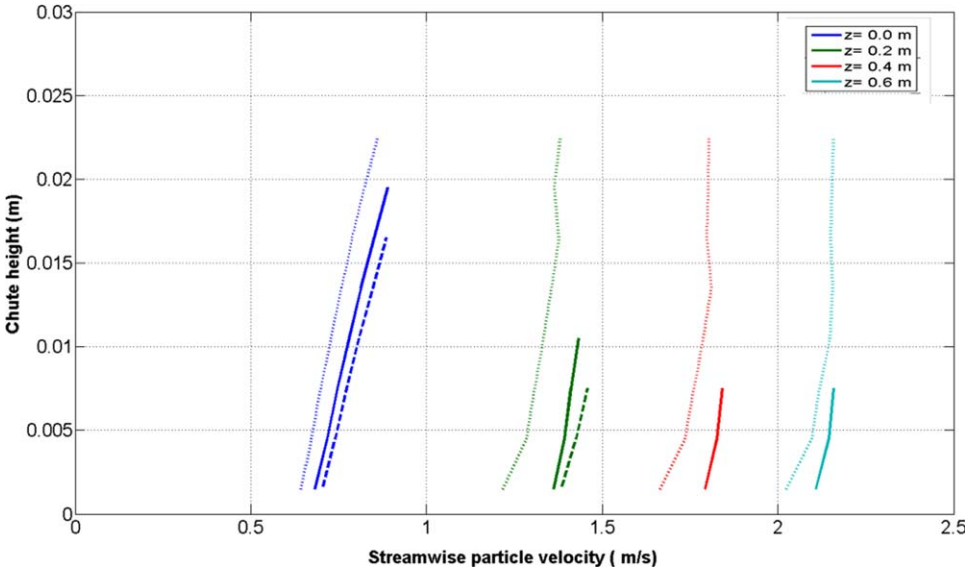

Figure 17. Average streamwise particle velocity along the depth of the chute for an inclination angle of 30°.

Solid lines: nonrotating chute. Dotted lines: left half of the chute for 16 rpm; dashed lines: right half of the chute for 16 rpm. [Color figure can be viewed in the online issue, which is available at wileyonlinelibrary.com.]

Streamwise surface velocity in the width-wise direction

Figures 13 and 14 show the streamwise surface particle velocity as a function of width-wise position at four different streamwise positions, for rotation rates 0 rpm (nonrotating chute), 4 rpm, 8 rpm, and 16 rpm. The streamwise positions are at $z = 0.0$ m, 0.2 m, 0.4 m, and 0.6 m. The simulation results (lines) are compared with experimental results (symbols). The figures show that in all cases the streamwise velocity is slightly lowered near the side walls of the chute. Moreover, as the rotation rate increases, the particles move sideways causing a lack of data at higher width-wise positions. Again, we find good agreement between the simulations and experimental results.

Spanwise surface velocity in the width-wise direction

Figure 15 illustrates the spanwise surface particle velocity along the width of the chute at different cross sections in the length of chute. The simulation results are compared with experimental results for different rotation rates of the chute at an inclination of 30°. We observe that the magnitude of the spanwise velocity first increases and then decreases for consecutive streamwise positions. This corresponds to the process of sideways motion induced by Coriolis forces, which is finally stopped by the compaction of the granular flow against the side wall. The maximum spanwise velocity increases with increasing rotation rate. Similar results, but with even larger spanwise velocities are found for a chute inclination angle of 40°, as shown in Figure 16. Again, some deviations between simulation and experiments are observed at the start of the chute ($z = 0$ m, blue symbols and blue lines) at higher rotation rates, consistent with our previous observation that the precise manner of particle introduction is important for the first 0.2 m. Taking this into account, rather good agreement is found between experiments and simulations.

Computational Measurements of Optically Inaccessible Properties

We have used the experiments on bed height and surface particle velocity to validate the DEM simulations. We now give two examples of how the simulations can be used to obtain insight in properties that cannot readily be obtained from optical experiments.

Depth-dependent flow profiles

The first example concerns the depth-dependent shear flow profile of a granular flow, that is, the streamwise velocity as a function of depth.

In Figure 17, we show the flow profiles for nonrotating (0 rpm) and rotating (16 rpm) chutes at different streamwise positions. The results for the nonrotating case have been averaged over the full width of the chute, whereas for the rotating case we have made two measurements, one averaging over the left half of the chute width and another averaging over the right half (excluding cells without particles). Figure 17 shows that in all cases the granular material behaves almost like a plug flow, with only a relatively small velocity gradient. In other words, the chute flow is dominated by slip with the bottom wall. This is consistent with our previous observation of the dominance of the coefficient of friction.

In the rotating chute, particles in the right half of the chute (as seen in the direction of flow) are slightly slowed down relative to a nonrotating chute. This may be caused by a dominance of the additional friction with the side wall induced by Coriolis forces over the centrifugal forces. Particles in the left half of the chute are not pushed against a side wall, and are therefore influenced more by the centrifugal forces, leading to a slight acceleration relative to a nonrotating chute.

Depth-dependent solid volume fraction

The second example of a property that is difficult to access experimentally is the depth-dependent solid

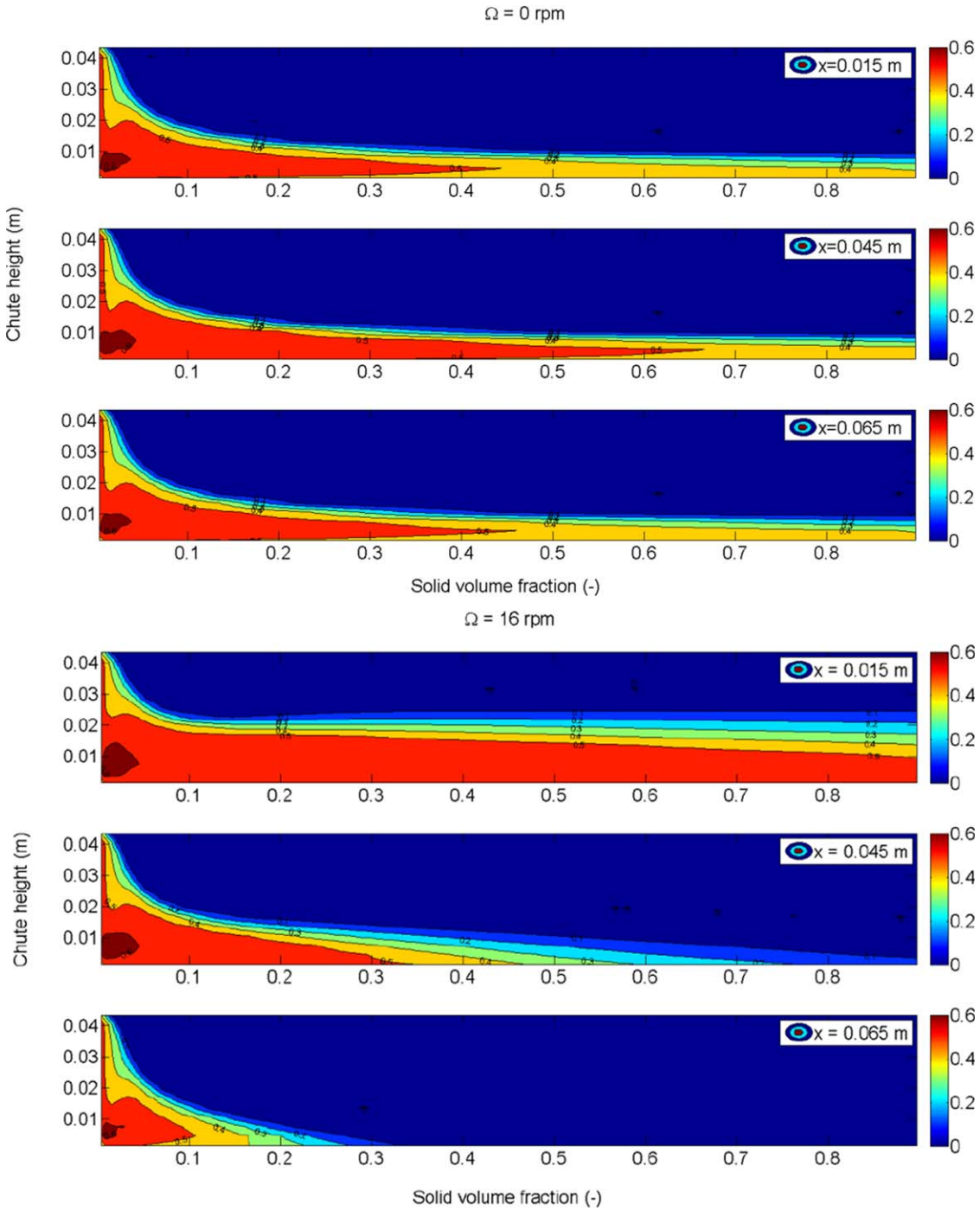

Figure 18. Contour plots of average solid volume fraction along the depth of the chute for an inclination angle of 30° and rotation rate of 0 rpm (top three panels), and 16 rpm (lower three panels).

Averages are taken over slices with a width of 0.025 m located at the left, center, and right side of the chute. [Color figure can be viewed in the online issue, which is available at wileyonlinelibrary.com.]

volume fraction. Figure 18 shows the contour plots of solid volume fraction as a function of the depth of the chute at different three width-wise positions. The simulation results shows that the bottom part of the granular flow in a chute is close to random close packing, but the solids volume fraction decreases toward the free surface, with the largest gradient near the free surface. The solid fraction is slightly different along the center line compared to the side positions for the nonrotating chute. For the case of rotation, the particles moves sideways which results in an increase in solid volume fraction on the right side of the chute. Measurements such as these are very difficult to obtain experimentally and show the complimentary strength of DEM simulations.

Conclusions

In this article, we have presented a comparative study of DEM simulations and experimental results of dry granular flows of 3-mm glass spheres down an inclined rotating chute.

The key objective of the work was to validate the model for granular flow on a rotating chute with experimental results of the bed height and surface particle velocity in the chute. We found that the precise inlet conditions are very important for the flow behavior in the initial part of the chute, but have no influence on the flow behavior after a relatively short distance from the inlet (in our case about 20 cm). We also found that the effect of air on the flow behavior of the particles is relatively small and can be captured effectively and efficiently by tuning the friction coefficient. For this type of chute flow, the most important particle contact parameters are the friction coefficient and, to a lesser extent, the rotational friction coefficient. The precise values of the normal and tangential coefficients of restitution have no discernible effect on the particle flow. The main effect of rotation is obvious, namely to push the particle stream against the side wall. However, in this work, we have shown that the simulation model is also capable of quantitatively predicting the experimental results. We have highlighted how the simulation model can subsequently be used to predict properties that are not readily accessible to optical experiments. We conclude that these simulations can be used with confidence to obtain more detailed insights in complex flows such as mixtures of particles of different size or different density. This will be the topic of our next article.

Acknowledgments

The authors acknowledge STW for financial support. The authors thank O. Bokhove, A. R. Thornton, and D. R. Tunuguntla for stimulating discussions.

Notation

Roman symbols

m = mass of particle, kg
$\boldsymbol{v}$ = particle velocity, m/s
$\mathbf{g}$ = gravitational acceleration, m/s^2
t = time, s
$\mathbf{F}$ = force, N
$\mathbf{T}$ = torque, Nm
$\mathbf{T}_r$ = rolling torque, Nm
I = moment of inertia, kg/m^2
$\mathbf{n}$ = normal unit vector
$\mathbf{t}$ = tangential unit vector
R_p = particle radius, m
R_r = rolling radius, m
D = diameter, m
$\mathbf{r}$ = position, m
Q = mass flow rate, kg/s
p = gas pressure, Pa
$\mathbf{u}$ = gas velocity, m/s
$\mathbf{S}_p$ = momentum source term, N/m^3
V = local volume of the computational cell, m^3
V_a = volume of particle, m^3
e = restitution coefficient
k = spring stiffness, N/m
NX, NY, NZ = number of grid cells in x, y, z direction
N = number of particles
A, B = constants
dt = time step

Greek symbols

$\boldsymbol{\omega}$ = rotational velocity, 1/s
η = damping coefficient
μ = coefficient of friction
μ_r = coefficient of rolling friction
β = interphase momentum transfer coefficient, kg/m^{3}s
θ = angle of inclination of the chute, degrees
ρ = density, kg/m^3
$\boldsymbol{\Omega}$ = rotation rate of chute, rad/s
ε = local porosity
$\boldsymbol{\tau}$ = gas-phase stress tensor, kg/ms^2
λ = gas-phase bulk viscosity, kg/ms
μ_g = gas-phase shear viscosity, kg/ms
δ = distribution function
$\boldsymbol{\delta}$ = overlap vector, m

Subscripts

a, b = particle indices
p = particle
g = gas phase
w = wall
n = normal
t = tangential
rel = relative
tot = total
g = gas

Superscripts

c = contact
p = pressure
d = drag
T = transposed

Literature Cited

1. Uhlmann M. An immersed boundary method with direct forcing for the simulation of particulate flow. *J Comput Phys*. 2005;209:448–476.
2. Roberts AW. Particle and bulk solids handling technology – bridging the theory practice gap. *Fifth World Congress on Particle Technology, Orlando, Florida, USA, CD-ROM proceedings*. 2006
3. Mio H, Komatsuki S, Akashi M, Shimosaka A, Shirakawa Y, Hidaka J, Kadowaki M, Matsuzaki S, Kunitomo K. Effect of chute angle on charging behavior of sintered ore particles at bell-less type charging system of blast furnace by discrete element method. *Iron Steel Inst Jpn Int*. 2009;49:479–486.
4. Zaimi SA, Campos T, Bennani M, Lecacheux B, Danloy G, Pomeroy D, Perez-Chust R. Blast furnace models development and application in Arcelor Mittal Group. *Revue de Metallurgie*. 2009;3:105–111.
5. Yu Y. Study and develop on the model for bell-less charging of blast furnace. M.Sc. Thesis. Chongqing, China: Chongqing University, 2008.
6. Nishimura T, Matsuzaki S, Shinotake A, Kunitomo K, Naito M. Development of mathematical model of blast furnace in Nippon Steel Corporation. In: Ariyama T, editor. *Recent Progress on Mathematical Modelling in Ironmaking*. Tokyo, Japan: The Iron and Steel Institute of Japan, 2008:6.
7. Ishida M, Shirai T. Velocity distributions in the flow of solid particles in an inclined open channel. *J Chem Eng Jpn*. 1979;12:46–50.
8. Augenstein DA, Hogg R. Friction factors for powder flow. *Powder Technol*. 1974;10:43–49.
9. Cundall PA, Strack ODL. A discrete numerical model for granular assemblies. *Geotechnique*. 1979;29:47–65.
10. Weinhart T, Thorton AR, Luding S, Bokhove O. Closure relations for shallow granular flows from particle simulations. *Granul Matter*. 2012;14:531–552.
11. Thorton AR, Weinhart T, Luding S, Bokhove O. Modeling of particle size segregation: calibration using the discrete particle method. *Int J Mod Phys*. 2012;C23:1240014.
12. Nouchi T, Sato T, Sato M, Takeda K, Ariyama T. Effects of operation condition and casting strategy on drainage efficiency of the blast furnace hearth. *Iron Steel Inst Jpn Int*. 2005;45:1515–1520.
13. Zhou Z, Zhu H, Yu A, Wright B, Pinson D, Zulli P. Discrete particle simulation of solid flow in a model blast furnace. *Iron Steel Inst Jpn Int*. 2005;45:1828–1837.
14. Mio H. Yamamoto K, Shimosaka A, Shirakawa Y, Hidaka J. Modeling of solid particle flow in blast furnace considering actual

operation by large scale dicrete element method. *Iron Steel Inst Jpn Int*. 2007;47:1745–1752.
15. Pinson D, Wright B. *Proceedings of the Discrete Element Methods*. Falmouth, UK: Minerals Engineering International (MEI), 2007.
16. Li Q, Feng MX, Zou ZS. Validation and calibration approach for discrete element simulation of burden charging in pre-reduction shaft furnace of COREX process. *ISIJ Int*. 2013;53(8):1365–1371.
17. Kou MY, Wu SL, Du KP, Shen W, Sun J, Zhang ZK. DEM Simulation of burden distribution in the upper part of COREX shaft furnace. *Iron Steel Inst Jpn Int*. 2013;53(6):1002–1009.
18. Hoomans PBP, Kuipers JAM, Briels WJ, Van Swaaij WPM. Discrete particle simulation of bubble and slug formation in a two dimensional gas-fluidised bed: a hard-sphere approach. *Chem Eng Sci*. 1996;51:99–118.
19. Van Der Hoef MA, Ye M, Van Sint Annaland M, Andrews AT IV, Sundaresan S, Kuipers JAM. Multi-scale modeling of gas-fluidized beds. *Adv Chem Eng*. 2006;31:65–149.
20. Godlieb W. High pressure fluidization. Ph.D. Thesis. Enschede, The Netherlands: Twente University, 2010.
21. Zeilstra C. Granular dynamics in vibrated beds. Ph.D. Thesis, Enschede, The Netherlands: Twente University, 2010.
22. Kano J, Kasai E, Saito F, Kawaguchi T. Numerical simulation model for granulation kinetics of iron ores. *Iron Steel Inst Jpn Int*. 2005;45: 500–505.
23. Stewart RL, Bridgwater J, Zhou YC, Yu AB. Simulated and measured flow of granules in a bladed mixer detailed comparison. *Chem Eng Sci*. 2001;56:5457–5471.
24. Di Maio FP, Di Renzo A, Trevisan D. Comparison of heat transfer models in DEM-CFD simulations of fluidized beds with an immersed probe. *Powder Technol*. 2009;193:257–265.
25. Kaneko Y, Shiojima T, Horio M. DEM simulation of fluidized beds for gas-phase olefin polymerization. *Chem Eng Sci*. 1999;54:5809–5821.
26. Nguyen VD, Cogné C, Guessasma M, Bellenger E, Fortin J. Discrete modeling of granular flow with thermal transfer: application to the discharge of silos. *Appl Therm Eng*. 2009;29:1846–1853.
27. Yu YW, Saxén H. Experimental and DEM study of segregation of ternary size particles in blast furnace top bunker model. *Chem Eng Sci*. 2010;65:5237–5250.
28. Yu YW, Saxén H. Discrete element method simulation of properties of a 3D conical hopper with mono-size spheres. *Adv Powder Technol*. 2011;22:324–331.
29. Mio H, Komatsuki S, Akashi M, Shimosaka A, Shirakawa Y, Hidaka J, Kadowaki M, Matsuzaki S, Kunitomo K. Validation of particle size segregation of sintered ore during flowing through laboratory-scale chute by discrete element method. *Iron Steel Inst Jpn Int*. 2008;48:1696–1703.
30. Zhang JY, Hu ZG, Wei G, Zhang YJ, Li TH, Li JH. Application of the discrete approach to the simulation of size segregation in granular chute flow. *Ind Eng Chem Res*. 2004;43:5521–5528.
31. Mio H, Komatsuki S, Akashi M, Shimosaka A, Shirakawa Y, Hidaka J, Kadowaki M, Matsuzaki S, Kunitomo K. Effect of chute angle on charging behavior of sintered ore particles at bell-less type charging system of blast furnace by discrete element method. *Iron Steel Inst Jpn Int*. 2009;49:479–486.
32. Sawley ML, Zaimi SA, Sert D. Study of the charging of a blast furnace with a rotating chute using the discrete element method. *Particle Based Methods II: Fundamentals and Applications*. Spain. International Center for Numerical Methods in Engineering (CIMNE), 2011.
33. Yu YW, Saxén H. Analysis of rapid flow of particles in and from an inclined chute using small-scale experiments and discrete element simulation. *Ironmaking Steelmaking*. 2011;38:432–441.
34. Yu YW, Saxén H. Flow of pellet and coke particles in and from a fixed chute. *Ind Eng Chem Res*. 2012;51(21):7383–7397.
35. Yu YW. Experimental and discrete element simulation studies of bell-less charging of blast furnace. Ph.D. Thesis. Abo, Finland: Abo Akademi University, 2013.
36. Shirsath SS, Padding JT, Deen NG, Clercx HJH, Kuipers JAM. Experimental study of monodisperse granular flow through an inclined rotating chute. *Powder Technol*. 2013;246:235–246.
37. Sakaguchi H, Ozaki E, Igarashi T. Plugging of the flow of granular materials during the discharge from a silo. *Int J Mod Phys*. 1993;B7: 1949–1963.
38. Beer FP, Johnson ER. *Mechanics for Engineer: Static and Dyanamics*. New York: MacGraw-Hill, 1973.
39. Zhou YC, Wright BD, Yang RY, Xu BH, Yu AB. Rolling friction in the dynamic simulation of sandpile formation. *Physica*. 1999;269: 536–553.
40. Van Heijst GJF, Clercx HJH. Laboratory modeling of geophysical vortices. *Annu Rev Fluid Mech*. 2009;41:143–164.
41. Kundu PK, Cohen IM. *Fluid Mechanics*, 4th ed. New York: Academic Press, 2008.
42. Goldschmidt MJV. Hydrodynamic modelling of fluidised bed spray granulation. Ph.D. Thesis. Enschede, The Netherlands: Twente University, 2001.
43. Beetstra R, Van der Hoef MA, Kuipers JAM. Drag force from lattice Boltzmann simulations of intermediate Reynolds number flow past mono- and bidisperse arrays of spheres. *AIChE J*. 2007;53: 408–501.
44. Laverman LA. On the hydrodynamics in gas phase polymerization reactors. Ph.D. Thesis. Eindhoven, The Netherlands: Eindhoven University of Technology, 2010.
45. Keane RD, Adrian RJ. Optimization of particle image velocimeters: II. Multiple pulsed systems. *Meas Sci Technol*. 1991;2:963–974.
46. Westerweel J. Fundamentals of digital particle image velocimetry. *Meas Sci Technol*. 1997;8:1379–1392.
47. Dijkhuizen W, Bokkers GA, Deen NG, van Sint Annaland M, Kuipers JAM. Extension of PIV for measuring granular temperature field in dense fluidized beds. *AIChE J*. 2007;53:108–118.
48. Alizadeh E, Bertrand F, Chaouki J. Comparison of DEM results and Lagrangian experimental data for the flow and mixing of granules in a rotating drum. *AIChE J*. 2014;60:60–75.
49. Müller CR, Holland DJ, Sederman AJ, Scott SA, Dennis JS, Gladden LF. Granular temperature: comparison of magnetic resonance measurements with discrete element model simulations. *Powder Technol*. 2008;184:241–253.
50. Müller CR, Scott SA, Holland DJ, Clarke BC, Sederman AJ, Dennis JS, Gladden LF. Validation of a discrete element model using magnetic resonance measurements. *Particuology*. 2009;7:297–306.

Manuscript received Nov. 15, 2013, and revision received May 16, 2014.